SINGLE LOOP PULSATING HEAT PIPE WITH NON-UNIFORM HEATING PATTERNS: FLUID INFRARED VISUALIZATION AND PRESSURE MEASUREMENTS

Daniele Mangini
University of Bergamo, Thermal Physics Laboratory, Via Galvani 2, Dalmine, Italy

Andreea Ioana Ilinca
Institute of Aerospace Thermodynamics, Pfaffenwaldring 31, 70569 Stuttgart

Mauro Mameli*, Davide Fioriti, Sauro Filippeschi
DESTEC, University of Pisa, Pisa, Italy
*mauro.mameli@ing.unipi.it

Lucio Araneo
Politecnico di Milano, Energy Department, via Lambruschini 4A, Milano, Italy

Marco Marengo
School of Computing, Engineering and Mathematics, University of Brighton, Lewes Road, BN2 4GJ Brighton, UK

Abstract. A novel Single Loop Pulsating Heat Pipe (SLPHP) filled at 60% filling ratio with pure ethanol, with an inner diameter of 2mm is tested in Bottom Heated mode varying the heating power. The system is designed with two sapphire tubes mounted between the evaporator and the condenser allowing simultaneous fluid flow high-speed visualizations and IR analysis. Furthermore, two highly accurate pressure transducers carry out local pressure measurements just at the ends of one of the sapphire inserts. Additionally, three heating elements are controlled independently, in such a way to heat up the device varying the distribution of the heating location at the evaporator. It is found that peculiar heating distributions promote the slug/plug flow motion in a preferential direction, increasing the overall performance of the device. Pressure measurements point out that the flow patterns are strictly related to the pressure drop between the evaporator and the condenser. Furthermore, the IR visualization highlights interesting phenomena related to the liquid film dynamics during the device operations, which represent a very useful information for future numerical modeling of Pulsating Heat Pipes.

Keywords: Pulsating Heat Pipe, Infrared Analysis, Flow patterns, Pressure measurement.

1. INTRODUCTION

As modern computer chips and power electronics become more powerful and compact, the need of more efficient cooling systems increases day by day. In the present scenario, Pulsating Heat Pipes (PHPs) are relatively new, wickless two-phase passive heat transfer devices that aim at meeting present and future thermal requirements (Akachi, 1990, 1993). Although the peculiar advantages of this emergent technology, such as its compactness, the possibility to dissipate high heat fluxes and the ability to work also in microgravity conditions, the PHPs governing phenomena are quite unique and not yet completely understood (Zhang and Faghri, 2008).

Since the Single Loop PHP (SLPHP) can be considered the basic constituent of a multi-turn Pulsating Heat Pipes, its full thermo-fluidic characterization is fundamental for the complete description of the PHP working principles. At present, several studies contribute to the understanding of SLPHP behavior (Khandekar and Groll, 2004, Khandekar et al. 2009, Spinato et al. 2015, Spinato et al. 2016), but further work is needed to evaluate the liquid film dynamics within PHPs, the presence of local dry-outs, eventual local thermodynamic non-equilibrium between the two-phases and the liquid film evaporation/condensation. In this regard, an Infrared (IR) analysis of the fluid flow may provide fundamental information. Actually, only few works in the literature investigate the distribution of temperatures on the external tube wall (Hemadri *et al.*, 2011; Liu *et al.*, 2012, Karthikeyan *et al.*, 2013; Karthikeyan *et al.*, 2014; Chauris *et al.*, 2015), but a direct flow IR analysis of the two-phase flow motion by means of IR transparent materials has not yet been performed in PHPs.

For these main reasons, a novel SLPHP is designed to perform the following simultaneous measurements: i) visualization of the fluid flow, ii) the fluid temperature distribution, iii) the liquid film dynamics during operation, iv) the instantaneous fluid pressure both in the heated and in the cooled section. Two transparent sapphire tubes connect the hot and the cold sections, allowing both high-speed visualization and IR analysis of the fluid flow and two high precision pressure transducers, mounted just before and after one of the sapphire inserts, allow to measure the local pressure in such points of the loop. Furthermore, a robust ground test characterization is performed, measuring the

external tube wall temperatures and calculating the overall thermal performance varying the heating power distribution at the evaporator.

Furthermore, the aim of the work is to provide useful information on the basic phenomena involved, improving the PHP understanding. It is intended to demonstrate the feasibility of a direct IR analysis on the fluid flow when the PHP is designed and assembled with transparent materials in the IR-spectrum. Since the most updated codes found in literature by the time being, do not completely consider the liquid film dynamics during PHP operations (Nekrashevych and Nikolayev, 2017; Manzoni *et al.*, 2016), such experimental analysis provides valuable information for developing of more accurate numerical codes on PHPs.

2. EXPERIMENTAL APPARATUS AND PROCEDURE

The basic features of the SLPHP are shown in Fig. 1. The evaporator and the condenser are made with copper tubes (inner diameter 2 mm, outer diameter 4 mm) in order to minimize the thermal resistance between the tubes and the heat source and heat sink. They are connected to two sapphire tubes (110 mm axial length, with the same ID and OD of the copper tubes) by means of brass joints and vacuum epoxy (Henkel Loctite® 9492). The sapphire transmissivity is equal to 0.9 in the mid-wave light spectrum (between 1 µm up to 5.5 µm). Twelve T-type thermocouples monitor the external wall temperature both in the heated and in the cooled section. Two high-accurate pressure transducers (Keller® PX33, 1 bar absolute, accuracy 0.05% FSO), mounted just before and after a sapphire insert, measure the pressure drop along the adiabatic section (190 mm axial length). The condenser section is embedded inside a mini shell and tube heat exchanger, connected to a thermal bath (Lauda® A300), that pumps directly water at 20 °C, with an accuracy of ±1 °C. The high-speed camera (Ximea® USB3 XIQ-093, resolution 1280x1024 pixel) records images up to 400 fps, while an high-speed and high resolution IR Camera (AIM® from TEC-MMG at ESA/ESTEC, spatial resolution 1280x1024) stores images up to 50 frames per second with a resolution of ±0.05 K. It is a middle-wave Infrared-camera (MWIR camera), with a bandwidth between 3 µm and 5µm. The optics is based on commercial lenses, with a transmissivity in such wavelengths of approximately 93%.

The SLPHP was first evacuated and then partially filled with degassed ethanol, with a volumetric ratio of 0.6 ± 0.025. Ethanol is chosen for both its fluid-dynamic and radiative properties in the IR spectrum.
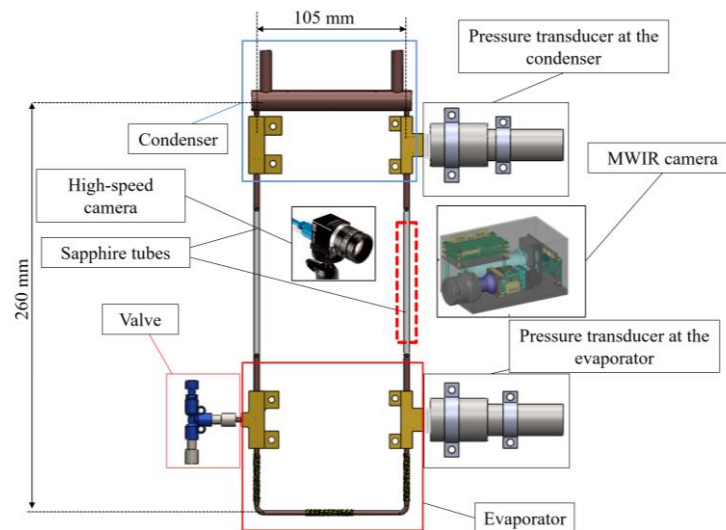

Figure 1. Main components of the SLPHP and thermocouples position. It is pointed out, with a dashed red rectangular contour, the sapphire section in which both high speed visualization and IR analysis are performed.

Three heating wires (Thermocoax®, Single core 1Nc Ac) are mounted at the evaporator section, providing a nominal wall-to-fluid heat flux of 6.5 W/cm^2 at 10 W. The heaters are controlled independently with a PWM control system, so as to vary the heating distribution along the heated zone. As shown in Fig. 2a, two heating elements (Heater A and Heater C) are positioned just above the 90° curves at the evaporator, in such a way to heat up the device non-symmetrically with respect to the gravity field, while the Heater B is mounted at the center of the evaporator horizontal section. As already demonstrated (Mangini *et al.*, 2016) for a similar multi-turn two-phase passive heat transfer device, heating up the device non-uniformly at the evaporator with specific heating configurations, a circulation in a preferential direction may be established, with a subsequent improvement of the overall thermal performance. The aim to control independently the three heating elements also in a SLPHP is to prove that also for a simplified geometry, a strategic heating distribution could establish a circulation in a preferential direction, thus improving the overall performance. Twelve T-type thermocouples measure the external wall temperature both in the heated and in the cooled

region of the single loop (see Fig. 2 B), while other two thermocouples monitor the environmental temperature during tests. The device is vacuumed by means of an ultra-high vacuum system (Varian® DS42 and TV81-T) down to 0.3 mPa and then it is partially filled up with the working fluid with a volumetric ratio of 0.6 ± 0.025(corresponding to 1.45 ml of ethanol). Finally, the micro-metering (Microcolumn ®) valve that connects the SLPHP to the device is closed, guarantying a leak down to 10^{-6} mbar/min.
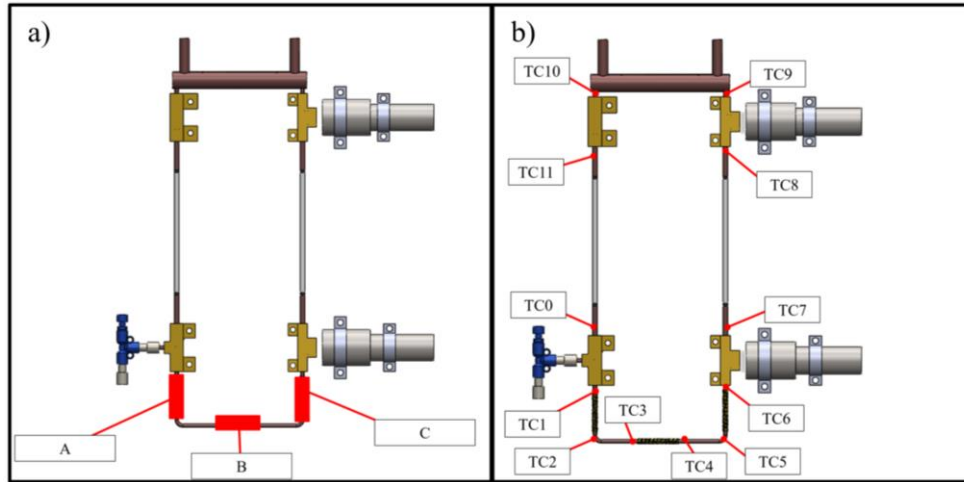

Figure 2. a) Heating element positon; b) Thermocouple positions

The fluid itself is previously degassed within a secondary tank, by continuous boiling and vacuuming cycles, as described by Henry et *al.*, 2004, in such a way to extract incondensable fluids before the filling operation. A data acquisition system (NI-cRIO-9074®, NI-9264®, NI-9214®, 2xNI-9205®, NI-9217®, NI-9472®) records the output of the thermocouples at 10 Hz, and the pressure transducers at 100 Hz. The high-speed camera is connected to an ultra-compact PC (NUC® Board D54250WYB) able to store images up to 100 fps, and it is synchronized via software with the pressure signals.

2. EXPERIMENTAL RESULTS AND PROCEDURE

The experimental campaign is carried out in order to point out:
- the effect of the heating distribution on the overall thermal performance;
- the operational regimes in terms of fluid motion;
- the relation between accurate local pressure measurements in the PHP section and the flow patterns observed through the transparent inserts;
- the IR analysis on the two-phase flow during PHP operations.

In the section 2.1 will be reassumed the influence of the heating distribution on the SLPHP performance and the local pressure measurements, while in the section 2.2 will be extensively discussed the more relevant results obtained by means of the direct two-phase flow IR analysis.

2.1. Thermal performances and pressure drop measurements

Tests are performed maintaining the environmental temperature at 20°C ±1°C, positioning the device vertically in Bottom Heated Mode, i.e. with the evaporator section below the condenser. The heating power is increased providing to the device a global heating power of 1 W, 3 W, 6 W, 12 W and 18 W. For all the global heating powers, except 1 W, different heating configurations are tested: the heating power is split between the three heaters, to vary the heating distribution. Pseudo-steady state conditions can be usually reached in approximately 3 min, due to the low thermal inertia of the system. Nevertheless, all the heating configurations have been kept constant for 15 minutes, to ensure that the device reaches for all the cases tested steady state conditions. A video sequence (20 s at 100 fps) is recorded during each combination of heat input power and fluid. The video acquisition starts 13 minutes after each heat input power variation. The equivalent thermal resistance (R_{eq}) is standardly evaluated as follows (Eq.1):

$$R_{eq} = \frac{(\bar{T}_e - \bar{T}_c)}{\dot{Q}_{tot}} \text{ (Eq. 1)}$$

Where: $\bar{T}_e, \bar{T}_c$ are respectively the average of the temperatures at the evaporator and at the condenser when pseudo-steady state conditions are reached, while $\dot{Q}_{tot}$ is the global heating power. Being the three heating elements in series,

the global heating power can be calculated as the sum of the heating power dissipated by the heater A ($\dot{Q}_A$), Heater B ($\dot{Q}_B$)and Heater C ($\dot{Q}_C$), as pointed out in the Eq. 2:

$$\dot{Q}_{tot} = \dot{Q}_A + \dot{Q}_B + \dot{Q}_C \qquad \text{(Eq.2)}$$

Since each of the three heating elements, being controlled independently, can provide different heating powers, the $\bar{T}_e$ needs to be calculated as pointed out in the Eq. 3:

$$\bar{T}_e = \frac{\dot{Q}_A}{\dot{Q}_{tot}}\max(T_1; T_2) + \frac{\dot{Q}_B}{\dot{Q}_{tot}}\max(T_3; T_4) + \frac{\dot{Q}_C}{\dot{Q}_{tot}}\max(T_5; T_6) \qquad \text{(Eq. 3)}$$

While the $\bar{T}_c$ is simply calculated averaging in time TC9 and TC10 when steady state conditions are reached.

The heating power is increased from 1 W to a global power of 18 W, varying the heating distribution along the three heating elements and testing different heating configuration. The overall temporal trend of the temperatures and the pressure recorded in the transparent section, and all the heating configurations are shown in Fig. 3. Only 1 W is not sufficient to activate a self-sustained two-phase flow within the loop: the temperatures at the evaporator increases, while the pressure, close to the saturation pressure of ethanol at 20°C, exhibits a flat trend. Increasing the power at 3 W (configuration 3A in Fig. 3A), the pressure signal displays some peaks, while the temperatures starts to decrease. In such period, the heating power activates a self-sustained two-phase flow motion, improving the heat transfer between the heated and the cooled section of the device. However, at 3 W only partial start-ups are detectable: the temperatures at the evaporator reside in a wide range of temperature and the heat transfer is not stable. Periods in which the two-phase flow oscillates between the heated and the cooled section are alternating with stop-over periods, where the fluid does not move, thus hindering the heat exchange. This is valid for all the configurations tested with a global heating input of 3 W (from 3a to 3e in Fig. 3 A), independently to the heating configuration.

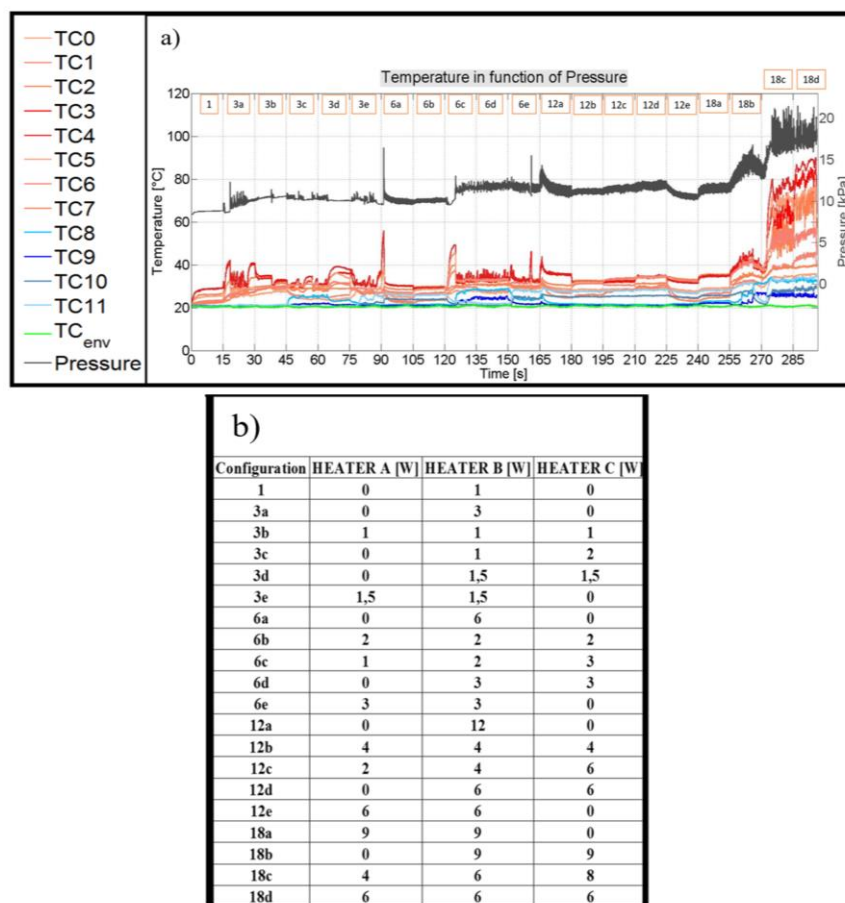| Configuration	HEATER A [W]	HEATER B [W]	HEATER C [W]
1	0	1	0
3a	0	3	0
3b	1	1	1
3c	0	1	2
3d	0	1,5	1,5
3e	1,5	1,5	0
6a	0	6	0
6b	2	2	2
6c	1	2	3
6d	0	3	3
6e	3	3	0
12a	0	12	0
12b	4	4	4
12c	2	4	6
12d	0	6	6
12e	6	6	0
18a	9	9	0
18b	0	9	9
18c	4	6	8
18d	6	6	6

Figure 3. A) Temperatures and pressure evolution during the long-time test; B) the heating configurations tested.

Providing to the device a heating power of 6 W to the Heater B (configuration 6a) a full start-up is detectable: after a sudden peak of pressure at the evaporator, the temperatures in the heated zone decrease abruptly at 35 °C. This results in an improvement of the thermal performance: the equivalent thermal resistance (R_{eq}) decreases down to 1 K/W, as observable in Fig. 4.

Interestingly, providing to the device the configuration 6a, a circulation of the two-phase flow that spontaneously follow a preferential direction is observable through the two transparent sections. The fluid visualization in Fig. 4 shows that an annular flow in the left transparent section flows continuously from the evaporator to the condenser, while a slug/plug flow that preferentially falls from the condenser is detectable in the right transparent insert. As a consequence, the TC10 and the TC11 have a higher value than the TC8 and the TC9, since the hot fluid from the evaporator is pushed preferentially through the left side of the loop. This circulation is obtained for the heating configurations 6a and 6b. Such two-phase flow motion in a preferential direction, continuously refreshing the hot section with a fluid flow that comes from the condenser with a lower temperature, improves the overall performance.

It is worthwhile to note that such circulation is achieved heating up the system with a symmetrical configuration. This could be explained because the SLPHP is very sensitive to small hydraulic non-symmetries and to the higher thermal inertia of the components at its right side, such as the two pressure stainless steel transducers with a total mass of 480 g. Providing to the device the heating configuration 6c, a sudden flow reversal is detectable: this time the annular flow that pushes directly the fluid from the evaporator to the condenser is visible through the right transparent section, while a slug/plug that goes preferentially from the evaporator to the condenser in the left one, as a sort of "anti-clockwise motion" (highlighted in the blue rectangular shape in Fig.4). This sudden variation of the circulation direction is due to the particular distribution of heating power provided by the configuration 6c: the local heating power provided to the Heater C is higher than the power dissipated by the Heaters A and B. Therefore, the fluid is pushed preferentially through the right channel, changing the overall circulation direction. Therefore, the TC8 and the TC9 are for such configuration higher than the TC10 and the TC11. The anti-clockwise circulation is also observable during tests performed with the configuration 6d: since the Heater A does not dissipate heating power, the fluid is not pushed through the left side of the loop to the condenser. Changing suddenly the heating power from the configuration 6d to the configuration 6e, the fluid returns to move almost instantaneously following a clockwise orientation. For the configuration 6d, the Heater C does not dissipate power, and therefore the fluid is not able to be pushed through the right side of the loop to the condenser. Interestingly, for such global heating power level of 6 W, the fluid motion is extremely sensitive to the heating distribution: a variation of the circulation direction is easily reachable providing a proper local heating power in the heated region.
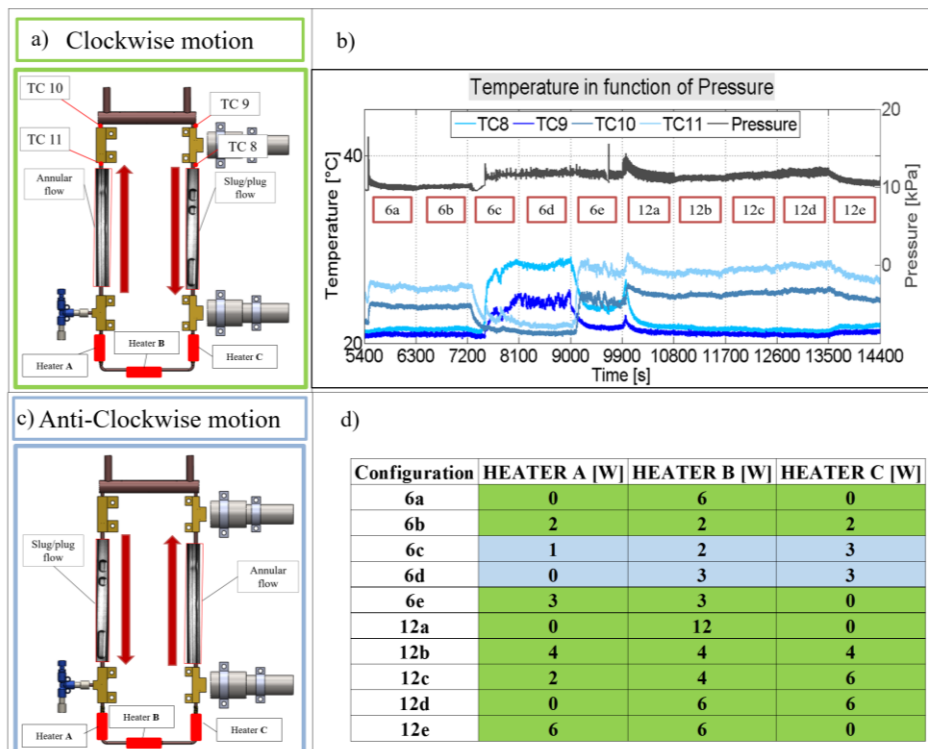

Figure 4. Directions of the flow circulation: a) clockwise motion, green color in table d); b) Anti-clockwise, blue color in Table d); c) temperatures and pressure in the condenser at 6 W and 12 W.

Increasing the global heating power from 6 W to 12 W (from the configuration 12a to the configuration 12e), the two-phase flow follows a clockwise direction, independently of the peculiar heating configuration at the evaporator. The TC10 and TC11 values are in fact every time higher than for TC9 and TC8 (Fig. 4), and the annular flow, pushing continuously the fluid from the heated to the cooled region, is always visible in the left transparent section. This could be due to the fact that increasing the global heat power input to dissipate, the fluid is thrusted more actively from the heated to the cooled section of the device, thus enhancing also the fluid inertia. Therefore, once the circulation is

established in the loop in a preferential direction, such inertial effect "dampens" the effect of the particular heating distribution provided at the evaporator, maintaining flow direction for all the following configurations.

Increasing further the global heating power from 12 W to 18 W, the temperatures at the evaporator increase, showing a thermal crisis (dry-out). Hence, the tests were stopped as soon as the temperatures at the evaporator reach 90°C in order to safely run the pressure transducers. At 18 W, the heat power is not able to change the fluid flow direction for the different configurations.

As soon as the configuration 18a is provided, the flow starts to oscillate without a preferential direction. In contrast with respect to the clockwise circulation for a global heating power of 12 W, for the configuration 18a the vapor expansion starts initially to push the fluid from the bottom right section. Nevertheless, it is not able to change completely the fluid circulation: hence the two-phase flow starts to oscillate, and both the two transparent inserts are characterized by an oscillating semi-annular flow. At high heating powers, any attempt to force a flow reversal by changing the heating distribution, when a net flow circulation is already established, fails due to a combination of inertial effects and distribution of the fluid phases. Indeed, the more heating power is provided, the higher the vapor fraction in the up-header, i.e. the heated branches in which the flow is pumped from the evaporator to the condenser, the higher quantity of fluid in the down-comer sections. It is more difficult for the vapor expansion to contrast liquid column pressure head and momentum. Therefore, only flow instabilities are detectable, i.e. an oscillating flow, thus severely decreasing the overall performance. Therefore, the R_{eq} increases for a global heating power of 18 W (Fig. 5).
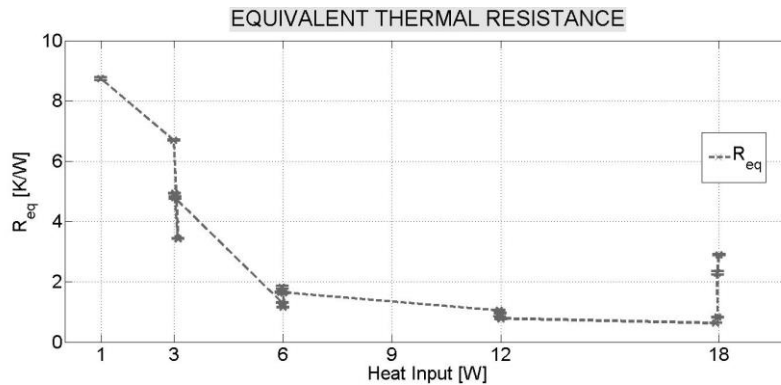

Figure 5. Equivalent thermal resistance for all the heating distribution tested

The thermal crisis observed providing to the device 18 W in Fig. 3 may be not related to a high amount of power. In order to prove this, an additional test is performed, in which 18 W are dissipated solely from the Heater B (Fig. 6), after the initiation of a self-sustained fluid flow circulation. The maximum temperatures reached with 18 W are approximately 40°C. The heat exchange is also stable: the temporal evolution of the temperatures during such test reside in a narrow range of temperatures after the start-up, and a fluid circulation in a preferential direction is detectable through the transparent inserts.

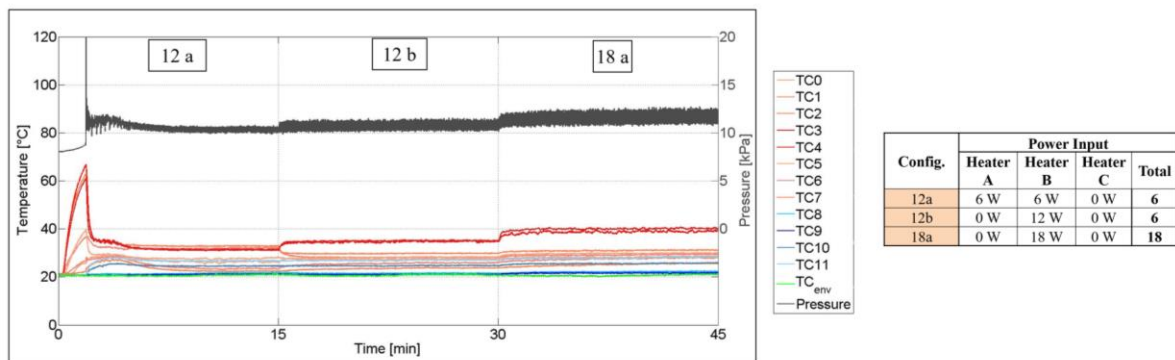| Config.	Power Input			
	Heater A	Heater B	Heater C	Total
12a	6 W	6 W	0 W	6
12b	0 W	12 W	0 W	6
18a	0 W	18 W	0 W	18

Figure 6. Test performed providing to the device 18 W solely at the heater B.

Furthermore, a synchronization between the images recorded in the transparent section and the pressure signals is performed and highlighted in Fig. 7. If a slug/plug flow is oscillating in the transparent section, the relationship between the fluid flow motion and the pressure measurements is clearly observable: when the two-phase flow is coming from the condenser section, the pressure decreases suddenly (sometimes of more than 500 Pa in less than 0.3 seconds) both at the evaporator and at the condenser. Nevertheless, when the flow is pushed from the heated to the cooled region during flow reversals, a sudden increase of pressure is measured both at the evaporator and at the condenser.

A direct interconnection is recognizable between the two local pressures recorded in the heated and in the cooled section in presence of a slug/plug flow: if the pressure at the evaporator increases/decreases, also the pressure at the condenser increases/decreases. Nevertheless, some differences can be found between these two measurements. More pronounced peaks of pressure are detectable closer to the evaporator rather than to the condenser.

The pressure drop is also calculated, simply subtracting the pressure at the evaporator to the pressure measured at the condenser (Fig. 7c). The pressure difference is characterized by some peaks when fluid flow accelerations are detectable through the transparent section. Nevertheless, the static pressure difference depends on three main terms, as highlighted in Eq. 4 (Collier and Thome, 1994):

$$\Delta P = \Delta P_f + \Delta P_a + \Delta P_g \tag{Eq. 4}$$

where $\Delta P_f, \Delta P_a, \Delta P_g$ are relatively the friction, acceleration and static head terms. The hydrostatic pressure is dependent by the void fraction along the tube in which the pressure measurements are performed, that continuously change in time during PHP operations and it is also dependent by the peculiar flow pattern observed. Further analysis is needed to calculate the magnitude of the three components in Eq. 4. For instance, having the possibility to test the device in microgravity by means of parabolic flights, the hydrostatic pressure could be neglected. Calculating the liquid velocity post-processing properly the images recorded in the transparent section, also the acceleration term can be estimated. In this way, it could be theoretically possible to calculate the pressure related to the skin friction, and correlating it with respect to the flow pattern observed.
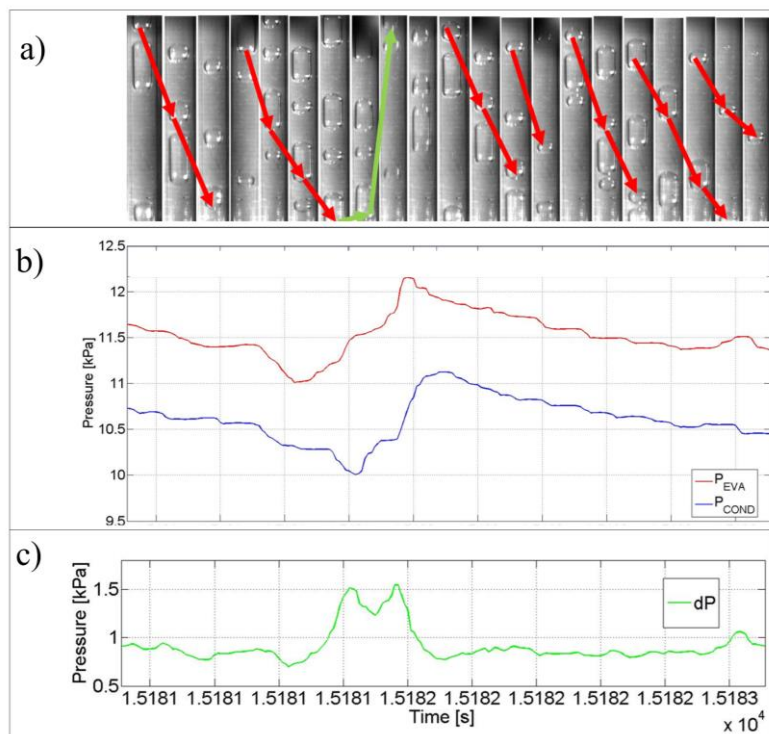

Figure 7. Flow visualization and pressure drop between a) the images obtained in the transparent section; b) pressure measurements at the evaporator (red line) and at the condenser (blue line). In c) the pressure drop measurements.

In case of annular flow, it is hard to find a relationship between the pressure measurements and the images recorded by the high-speed camera. In fact, it is difficult to catch the annular flow evolution solely with the high-speed camera, since there are no liquid menisci to track as in the slug/plug flow case. Nevertheless, the IR analysis performed and extensively discussed in the next section provides also for the annular flow additional information regarding the liquid film dynamics. However, some aspects regarding the fluid-dynamic of the annular flow can be understood observing the pressure signals during tests. The pressures measured when an annular flow pattern is observable (Fig. 8b) and its pressure drop (Fig. 8d) are completely different with respect to the slug/plug flow case (Fig. 8a and Fig. 8c respectively): The oscillations have a higher frequency in time for the annular flow.
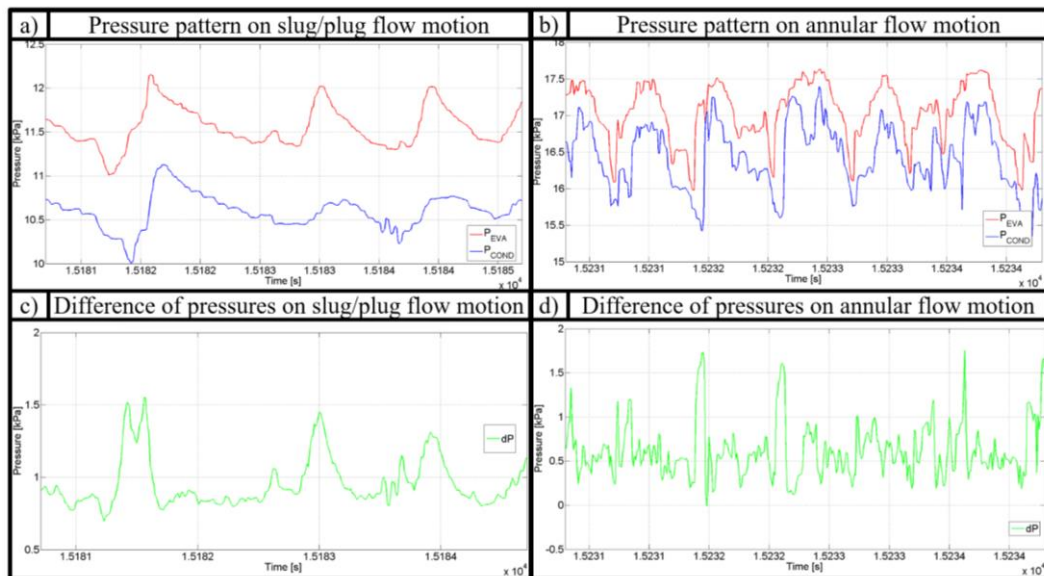
Figure 8. a) Pressure recorded in the heated (red line) and in the cooled region (blue line) in the case of a) slug/plug flow and b) annular flow. Pressure drop measurements (green line) in the case of c) slug/plug flow and d) annular flow.

2.2. IR analysis

The IR analysis is performed for two main reasons:
1) Check the feasibility of IR visualization on a PHP made with transparent tubes in the IR-spectrum (i.e. sapphire);
2) Provide additional information on the thermo-fluid dynamics of a PHP with a simplified geometry during its operation.
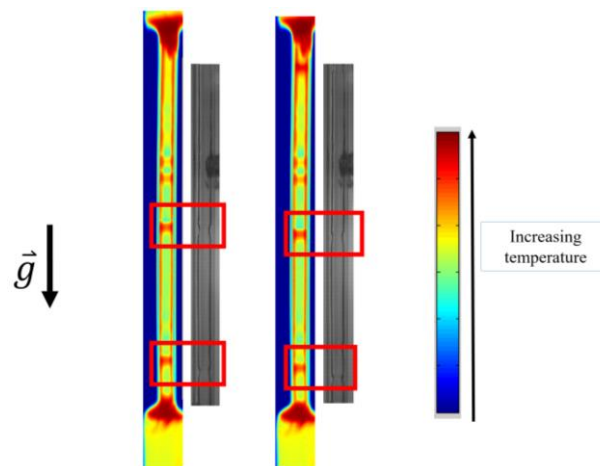
Figure 9. Two consecutive images temporally spaced at 0.02 seconds and their corresponding visual images. The emissivity depends on the liquid thickness.

The IR camera is positioned just in front of one of the sapphire inserts. IR-images are recorded at 50 fps, and they are synchronized in time with the images stored by the high-speed camera and the pressure signals. IR-images are collected for 20 consecutive seconds. A tank filled up with water at 15°C is positioned just behind the sapphire tube, in such a way to improve the contrast between the tube itself and the background. Since ethanol is a semi-transparent fluid between 1 μm and 5 μm, its global emissivity ε does not depend only on the temperature, but also on the liquid thickness. Sobac and Brutin, 2012, measured the global emissivity of ethanol between 1 μm and 5 μm as a function of the liquid thickness by means of a spectrophotometer.

When an annular flow is passing through the sapphire insert, it is possible to qualitatively detect the liquid film thickness variations. This is clearly observable from the Fig. 10: in the regions in which the liquid film attached on the wall is thicker (highlighted with red rectangular shapes in Fig. 10), the local temperature detected by the camera has a higher value. Such IR output is likely related to the decrease of transmissivity when the inner sapphire wall is covered

by a thicker liquid film, and not for its higher temperature. Therefore, it is possible to detect the liquid film evolution when annular flow is present in the tube.

Furthermore, the position of the liquid/vapor interface for a slug/plug flow regime is not detected properly by the IR-camera only (Fig. 11). At the interface, the thickness of the liquid phase is dependent by a number of parameters, such as its motion along the tube and bubble coalescence (Tong et al., 2001). For these reasons the IR analysis is potentially able to provide quantitative temperature analysis only if the liquid thickness is a-priori known (for example in case the whole tube is filled by the liquid phase). Otherwise, in case of annular flows, only qualitative flow motion analysis is possible using a direct measurement.

During the post-processing, both the IR-images and the images recorded by the high-speed camera are correlated and synchronized with respect to the pressure signals. The coupled IR and high speed images firstly point out the feasibility to detect the liquid film evolution during PHP operations within the sapphire inner wall. In fact, the vapor bubbles and the sapphire insert itself, being highly transparent in the IR-spectrum (almost 90% of transparency in the IR-spectrum), are not influencing the IR camera acquisition (Fig. 11). Zooming to the liquid/vapor interface (yellow rectangular section in Fig. 11), it is clearly observable that the IR images cut off such interface: in such region, where the liquid film thickness is different, the local transmissivity variation creates a squared shape in the visual representation.
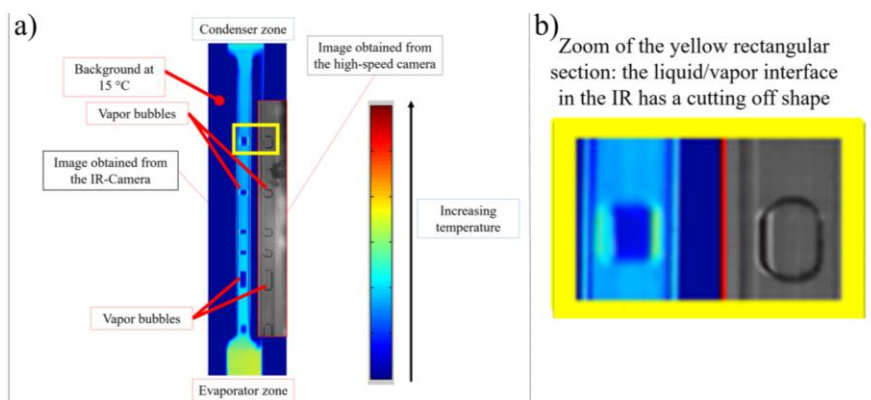

Figure 10. a) Slug-plug image obtained from the IR and the high-speed visualization; b) Zoom of the yellow section.

During the start-up, the liquid temperature close to the evaporator starts to increase (Fig. 12). The slug/plug flow motion, observable both by the high-speed images and IR camera, starts to oscillate in the sapphire insert. During the first seconds, only some oscillations of the slug/plug flow motion are detectable by the high-speed camera. Nevertheless, looking at the IR images, it is recognizable a continue increase of temperature of the liquid phase close to the evaporator. Such slug/plug flow oscillations become more and more vigorous, until an intense acceleration of the two-phase flow changes the flow pattern from a slug/plug flow to an annular flow.
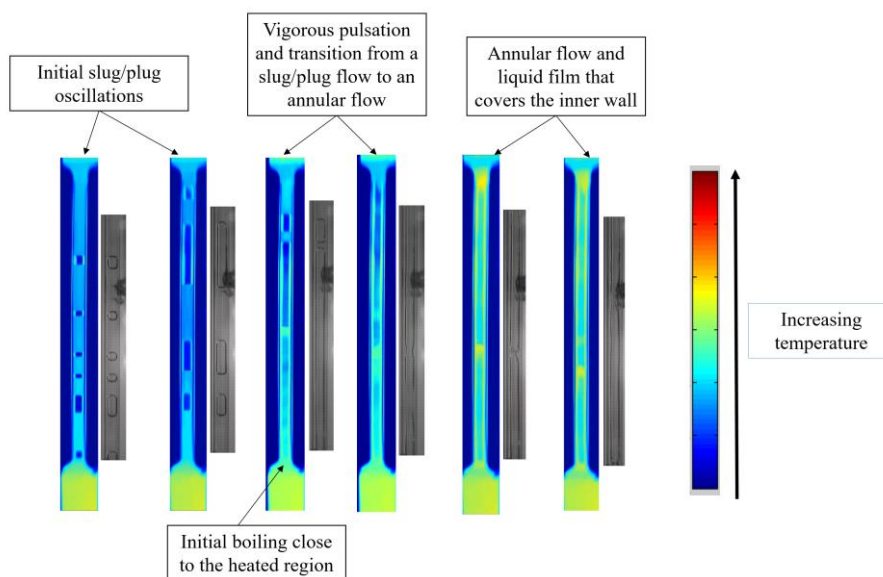

Figure 11. More relevant events observed during the start-up providing to the device a local heating power of 6 W just below the sapphire insert.

As soon as the annular flow is detectable in the sapphire section, the variation of temperature between the tube ends become smaller: the annular flow, pushed forcefully from the evaporator, acts as a sort of thermal vector able to release heat from the heated to the cooled region almost instantaneously. Furthermore, as soon as the annular flow is visible from the transparent section, the liquid film starts to cover entirely the inner wall. In fact, the IR camera does not anymore detect the lower background temperature, but a liquid film that continuously wet the inner part of the tube.
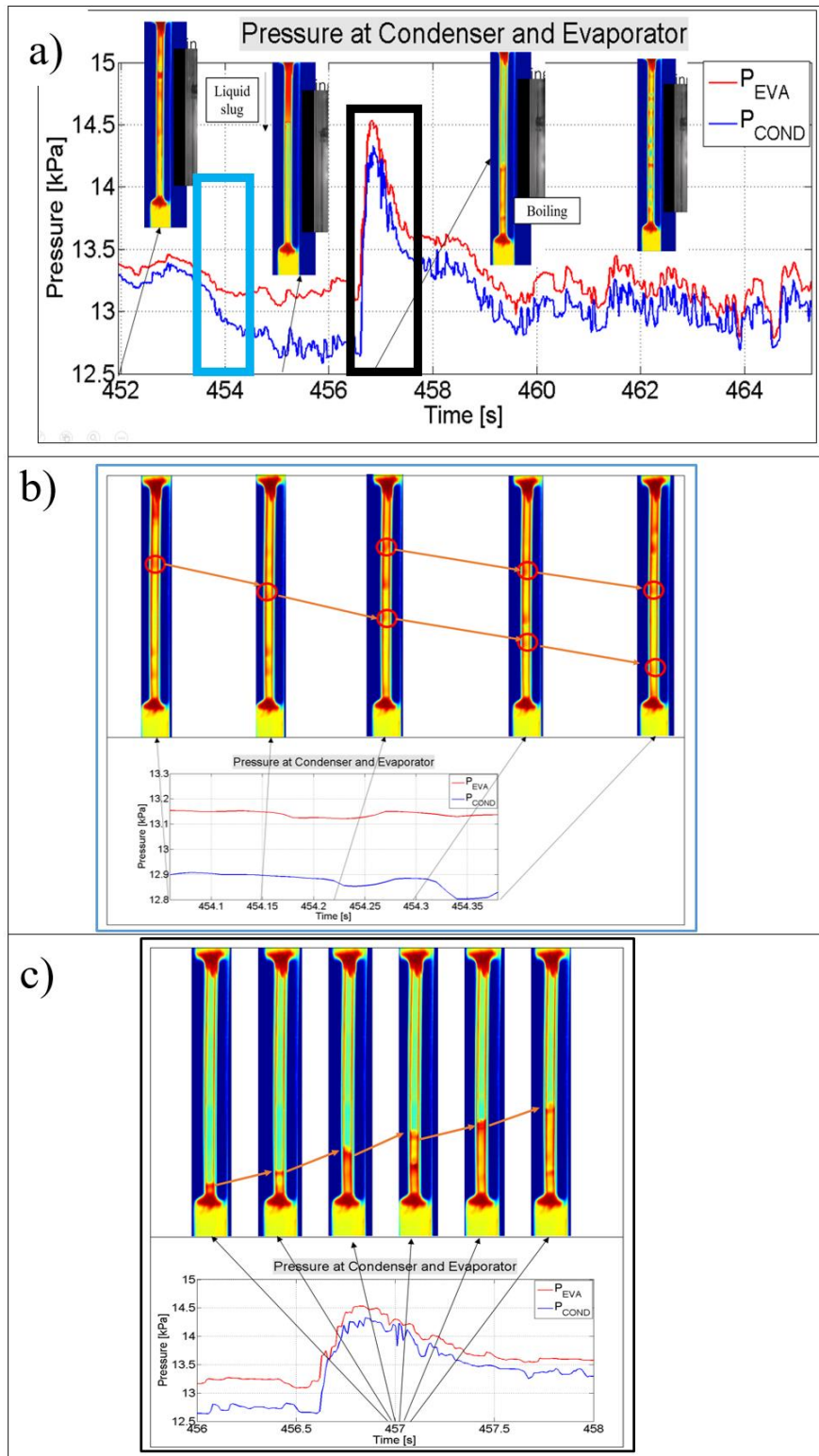

Figure 12. a) Synchronized pressure signals and IR images when the flow is oscillating in the loop. b) Zoom of the blue rectangular shape in a); c) Zoom of the black rectangular shape in a).

A semi-annular flow pushed from the evaporator to the condenser is usually observed when the fluid is oscillating in the loop. Interestingly, the liquid film is pushed from the cooled to the heated section by gravity when there are no increases of pressure at the sapphire tube ends (rectangular section in Fig. 13). From the IR images, it is observable the liquid film that falls from the condenser through the inner part of the tube thanks to gravity, similar to what happens in two phase thermosyphons (blue rectangular shape in Fig. 13). During such flow patterns, it is sometimes also recognizable a liquid slug that is pushed from the condenser to the evaporator by gravity. When such liquid slug reaches the heated section, boiling is observable in the region close to the evaporator: An annular flow is strongly pushed from the evaporator to the condenser, while a sudden variation of pressure of almost 1.5 kPa is measured from both the transducers (black rectangular section in Fig. 13). From that moment, an annular flow is continuously visible inside the sapphire insert.

3. CONCLUSIONS

A Single Loop Pulsating Heat Pipe, filled up with pure, degassed ethanol (60% FR) with an inner diameter value of 2 mm is tested in Bottom Heated mode varying the heat power level and spatial distribution. Three heating elements are controlled independently to heat up the device. With respect to previous SLPHP experiments in literature, such device is designed with two sapphire inserts mounted between the evaporator and the condenser. The sapphire tubes, being almost transparent in the MWIR spectrum, allows a qualitative IR analysis of the inner two-phase flow motion. Furthermore, two highly accurate pressure transducers measure the pressure just at the ends of one of the sapphire inserts.

Results point out that also for a single turn PHP peculiar heating configurations stabilize the two-phase flow motion in a preferential direction, thus improving the overall performance. The pressure measurements recorded both in the heated and in the cooled section highlights that the pressure evolution is strictly dependent on the observed flow pattern. When a slug/plug flow is observable through the transparent section between the two pressure transducers, the difference of pressure reaches 1.5 kPa and the pressure oscillations exhibit a lower frequency. On the contrary, when an annular flow is visible, the pressure variations between the heated and the cooled section are less than the slug/plug flow case, but with higher frequency. The pressure drop is simply calculated with the difference between the pressure recorded in the heated and in the cooled section. Nevertheless, being such measurements dependent on the hydrostatic pressure, i.e. the local vapor quality, the saturation pressure at the evaporator and at the condenser, the fluid momentum, and the friction losses, further analysis is needed to provide quantitative data on the pressure components.

Furthermore, the present work points out the possibility to visualize by means of a MWIR camera the liquid flow evolution within sapphire inserts during PHP operations. The IR images, together with the synchronized images recorded by a high-speed VIS camera, are able to support the detection and the understanding of the flow regime physics, such as wetting and de-wetting, and boiling phenomena. For example, in the presence of na annular flow, the liquid film can be pushed back to the evaporator because of gravity. During the start-up, a liquid film surrounds the inner wall as soon as boiling conditions are reached.

Presently, there are still limitations in such IR analysis. For example, the structure and the dynamics of the liquid/vapor interfaces are poorly measurable, being the IR transmissivity of the ethanol film dependent also on its unknown thickness. Nevertheless, such IR visualizations, coupled with high speed images and highly accurate pressure measurements, could provide useful information for validating the actual lumped parameters models (Nikolayev et al. 2017, Manzoni et al. 2016) and the emerging CFD simulations of PHPs (Jiaqiang et al. 2015, Pouryoussefi and Zhang 2015).

5. REFERENCES

Akachi, H., 1990, Structure of a heat pipe *US Pantent* 4.921.041.
Akachi, H., 1993, Structure of a micro heat pipe *US Patent* 5.219.020.
Charoensawan, P., Khandekar, S., Groll, M., Terdtoon, P., Closed loop pulsating heat pipes Part A: parametric experimental investigations; *Applied Thermal Engineering*, Vol. 23, pp. 2009-2020.

Chauris, N., Ayel, V., Bertin, Y. and Romestant, C., 2015. "Evaporation of a liquid film deposited on a capillary heated tube: Experimental analysis by infrared thermography of its thermal footprint". *International Journal of Heat and Mass Transfer*, Vol. 86, pp. 492-507.

Collier G., Thome J.R., 1994 Convective boiling and condensation, *Oxford Science Publications, third edition.*

Hemadri, V.A., Gupta, A. and Khandekar, S., 2011. "Thermal radiators with embedded pulsating heat pipes: Infra-red thermography and simulations". *Applied Thermal Engineering*, Vol. 31(6-7), pp. 1332-1346.

Henry, C.D, Kim, J., Chamberlain, B., 2004, "Heater size and heater aspect ratio effects on sub-cooled pool boiling heat transfer in low-g, 3rd International Symposium on Two-Phase Flow modeling and Experimentation", Pisa.

Jiaqiang, E., Zhao, X., Deng, Y., Zhu, H, 2015. "Pressure distribution and flow characteristics of closed oscillating heat pipe during the starting process at different vacuum degrees", *Applied Thermal Engineering* Vol. 93, pp. 166–173.

Karthikeyan, V.K., Khandekar, S., Pillai, B.C. and Sharma, P.K., 2014. "Infrared thermography of a pulsating heat pipe: Flow regimes and multiple steady states". *Applied Thermal Engineering*, Vol. 62(2), pp. 470-480.

Karthikeyan, V.K., Khandekar, S., Pillai, B.C. and Sharma, P.K., 2013. "Infrared thermography of a pulsating heat pipe: Flow regimes and multiple steady states". *Applied Thermal Engineering*, Vol. 61(2), pp. 470-480.

Khandekar, S., Groll, M., 2004, An insight into thermo-hydrodynamic coupling in closed loop pulsating heat pipes, *International Journal of Thermal Sciences*, Vol. 43, pp. 13-20.

Khandekar, S., Gautam, A.P., Sharma P., 2009. "Multiple quasi-steady states in a closed loop pulsating heat pipe". *International Journal of Thermal Sciences*, Vol. 48, pp. 535–546

Liu, X., Wang, C. and Chen, Y., 2016. "Analysis of operation and heat transfer characteristics in pulsating heat pipe based on infrared thermal imaging technology". *Huagong Xuebao/CIESC Journal*, Vol. 67(4), pp. 1129-1135.

Mangini, D., Mameli, M., Fioriti, D., Filippeschi, S., Araneo, L., Marengo, M., 2017, "Hybrid Pulsating Heat Pipe for space applications with non-uniform heating patterns: ground and microgravity experiments", *Applied Thermal Engineering*, Article in Press.

Manzoni, M., Mameli, M., de Falco, C., L. Araneo, Marengo, M., (2016), "Advanced numerical method for a thermally induced slug flow: application to a capillary Closed Loop Pulsating Heat Pipe", *International Journal for Numerical Methods in Fluids*

Nekrashevych, I., Nikolayev, V. S., 2017 "Effect of tube heat conduction on the pulsating heat-pipe start-up", *Applied Thermal Engineering*, Vol. 117, pp. 24-29.

Pouryoussefi, S.M. and Zhang Y., 2015. "Numerical investigation of chaotic flow in a 2D closed-loop pulsating heat pipe", *Applied Thermal Engineering,* Vol. 98, pp. 617-627.

Sobac, B., Brutin, D., 2012, "Thermocapillary instabilities in an evaporating drop deposited onto a heated substrate", *Physics of Fluids*, Vol. 24.

Spinato, G., Borani, N., Thome, J.R., 2015 "Understanding the self-sustained oscillating two-phase flow motion in a closed loop pulsating heat pipe", *Energy*, Vol. 90, pp. 889–899.

Spinato, G., Borani, N., Thome, J.R., 2016 "Operational regimes in a closed loop pulsating heat pipe", *International Journal of Thermal Sciences*, Vol. 102, pp. 78–88.

Tong, B.Y., Wong, T.N., Ooi, K.T., 2001, "Closed Loop Pulsating Heat Pipe", *Applied Thermal Engineering*, Vol. 21, pp. 1845-1862.

Zhang, Y., Faghri, A., 2008, "Advances and unsolved issues in pulsating heat pipes", *Heat Transfer Engineering*, Vol. 29, pp. 20-44.